

The structure of molecular gas associated with NGC 2264: wide-field ^{12}CO and H_2 imaging

J. V. Buckle^{1,2*}, J. S. Richer^{1,2} and C. J. Davis³

¹*Cavendish Astrophysics Group, JJ Thomson Avenue, Cambridge, UK*

²*Kavli Institute for Cosmology Cambridge, Madingley Road, Cambridge, UK*

³*Joint Astronomy Centre, University Park, Hilo, Hawaii, USA*

Accepted . Received ; in original form

ABSTRACT

We present wide-field, high-resolution imaging observations in ^{12}CO 3 \rightarrow 2 and H_2 1–0 S(1) towards a ~ 1 square degree region of NGC 2264. We identify 46 H_2 emission objects, of which 35 are new discoveries. We characterize several cores as protostellar, reducing the previously observed ratio of prestellar/protostellar cores in the NGC 2264 clusters. The length of H_2 jets increases the previously reported spatial extent of the clusters. In each cluster, $<0.5\%$ of cloud material has been perturbed by outflow activity. A principal component analysis of the ^{12}CO data suggests that turbulence is driven on scales >2.6 pc, which is larger than the extent of the outflows. We obtain an exponent $\alpha=0.74$ for the size-linewidth relation, possibly due to the high surface density of NGC 2264. In this very active, mixed-mass star forming region, our observations suggest that protostellar outflow activity is not injecting energy and momentum on a large enough scale to be the dominant source of turbulence.

Key words: ISM: jets and outflows – infrared: ISM – submillimetre – stars: formation

1 INTRODUCTION

Studies of young clusters are essential for understanding star formation, since most stars, and especially massive stars, are known to form in clusters (Zinnecker & Yorke 2007). NGC 2264 is an attractive target for studying this mode of star formation, since it is nearby, has relatively low foreground extinction and there is a large population of pre-main sequence stars, whose age spread is evidence of sequential star formation (Adams, Strom & Strom 1983). The region contains a wealth of submm cores (Ward-Thompson et al. 2000), pre-main sequence stars and protostellar sources (Young et al. 2006; Teixeira et al. 2006), many of which have formed in clusters (Wolf-Chase et al. 2003; Fűrész et al. 2006; Young et al. 2006). At 760–900 pc distance (see Baxter et al. 2009, and references therein for discussion), the region contains over 300 Class II objects, and 30 Class I objects (Dahm & Simon 2005). Several young Class 0 objects have been identified (Teixeira et al. 2006; Fűrész et al. 2006; Peretto, André & Belloche 2006). Kinematic motions include large-scale infall motions (Peretto et al. 2006; Williams & Garland 2002), and large, fast outflows, including the well-known NGC 2264 G (Lada & Fich 1996; Hedden et al. 2006). The wide field optical images of Reipurth et al. (2004) reveal a number of HH objects, several of which trace giant, parsec-scale outflows. Published infrared images of the NGC 2264 region cover only very small areas; maps of the NGC 2264 G molecular out-

flow (MHO 1358/1359¹) have been presented by Davis & Eisloffel (1995), while more recently a number of H_2 features (MHO 1349–1359) have been identified around NGC 2264 C by Wang et al. (2002).

Outflows have a significant impact on material within the parent molecular cloud, injecting energy and momentum at large distances. The outflows extend typically over 0.1–1 parsec, and the combined sub-arcsecond resolution H_2 images with deep spectral imaging in ^{12}CO , result in a more complete census of star formation activity in clustered regions. Outflow kinetic energies can be comparable to, or even larger than, turbulent and gravitational energies of natal clouds, and could have a significant disruptive effect (McKee & Ostriker 2007). In order to find evidence for, and quantify the disruptive effects of molecular outflows, it is crucial to map the entire cloud.

Fig. 1 shows the Digitized Sky survey (DSS) optical image of NGC 2264, with the main star formation regions and nebulae labelled, obtained with Starlink Gaia using Skycat². A detailed review of this region has been published by Dahm (2008). We present wide field, high resolution mapping observations of NGC 2264. Through CO observations we can provide a complete census of outflow activity in the region, investigating any dynamic impact

¹ The MHO (Molecular Hydrogen emission-line Object) catalogue is maintained at <http://www.jach.hawaii.edu/UKIRT/MHCat/>

² <http://archive.eso.org/cms/tools-documentation/skycat>

* E-mail: j.buckle@mrao.cam.ac.uk

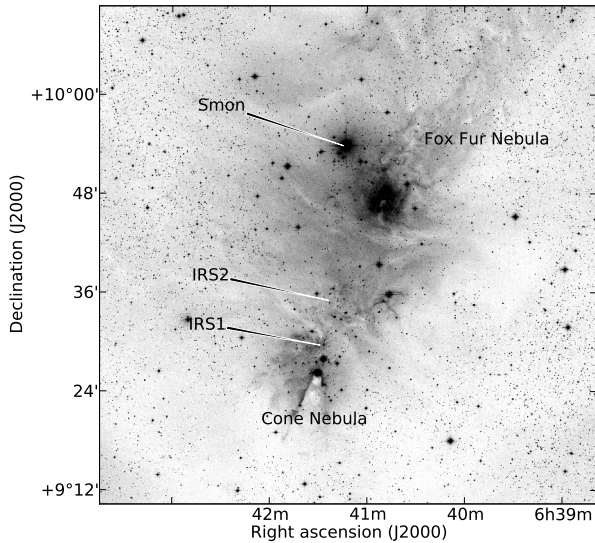


Figure 1. DSS optical image of NGC 2264 (the Christmas Tree Nebula) showing the massive O star S Mon, the two star-forming clusters NGC 2264 C (also known as Allen’s Source, and IRS1) and NGC 2264 D (also known as IRS2), and the two nebulae within the cloud, the Cone Nebula and the Fox Fur Nebula.

the outflows are having on the parent molecular cloud through energy injection. Using H_2 narrow line imaging, we can detect the youngest flows, from emission arising in gas shocked by the impact of protostellar outflows, and measure the extent of these flows by tracing the detected emission knots and HH objects.

2 DESCRIPTION OF OBSERVATIONS

2.1 Spectral Line Observations

The spectral-line observations were taken at the JCMT (James Clerk Maxwell Telescope) using HARP (Heterodyne Array Receiver Programme, Buckle et al. 2009). Observations of CO $3 \rightarrow 2$ at 345.796 GHz were taken with a 0.488 MHz (0.423 km s^{-1}) spectral resolution and gridded with $6''$ spatial pixels. The beam size is $14''$ at 345 GHz. The map covers an area of 1 square degree, and observations totalling 12.9 hours were taken during August and October 2007, in position-switch raster mode. The observations were taken in Band 3 weather, with zenith opacity values between 0.13 and 0.19, and average system temperatures $\sim 550 \text{ K}$. Averaged over emission free regions of the map, a 1σ rms of 0.32 K per pixel in 1.0 km s^{-1} spectral channels was obtained.

All intensities reported here are in units of T_A^* , the antenna temperature corrected for sky and telescopes losses (Kutner & Ulich 1981). The main beam brightness temperature, $T_{mb} = T_A^*/\eta_{mb}$, with a main beam efficiency, $\eta_{mb} = 0.66$. Frequent pointing and focus observations were carried out, and calibration observations using N2071IR. The scatter in these observations suggest a calibration accuracy of $\sim 20\%$.

The data were reduced and analyzed using the Starlink project software, in particular SMURF (Jenness et al. 2008) and KAPPA (Currie et al. 2008) routines.

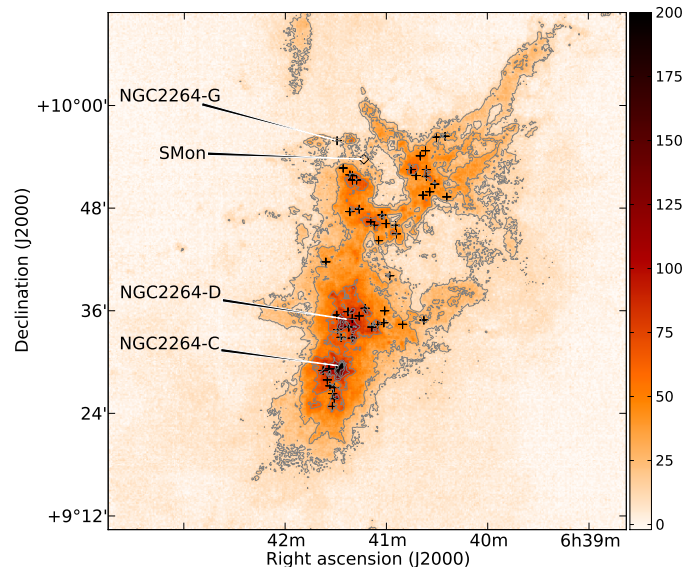


Figure 2. Integrated CO intensity map of NGC 2264, in the velocity range -20 to 30 km s^{-1} , with contours at 15,30,60,90,120,150 K km s^{-1} . A diamond marks the position of S Mon. Crosses mark dense cores identified through SCUBA observations (Di Francesco et al. 2008). Labels mark the well-known protostar NGC 2264 G, and the two star-forming clusters NGC 2264 C and NGC 2264 D.

2.2 H_2 Imaging Observations

The infrared imaging observations were taken at UKIRT (the United Kingdom Infrared Telescope) using the near-IR wide-field camera WFCAM (Casali et al. 2007). The observations cover an area on sky of 0.75 sq. degrees (a WFCAM ‘tile’), with a pixel size of $0.2''$. Images were obtained through broad-band K ($\lambda = 2.20 \mu\text{m}$, $\delta\lambda = 0.34 \mu\text{m}$) and narrow-band H_2 ($\lambda = 2.121 \mu\text{m}$, $\delta\lambda = 0.021 \mu\text{m}$) filters. Exposure times of 5 sec and 40 sec were used; thus, the total per-pixel integration times were 100 sec and 800 sec in K and H_2 , respectively.

Data were initially reduced by the Cambridge Astronomical Survey Unit (CASU), and distributed through the Wide Field Astronomy Unit (WFAU) archive. Further data reduction and analysis was carried out using Starlink KAPPA routines (Davis et al. 2009).

2.3 Data Summary

The two datasets presented here probe the most active regions of current star formation. CO $3 \rightarrow 2$ emission traces dense, warm gas typical in regions of star formation, with temperatures $10\text{--}50 \text{ K}$ and gas densities of $10^4\text{--}10^5 \text{ cm}^{-3}$. The higher critical density of the $3 \rightarrow 2$ line over lower excitation lines makes this transition a useful tool for tracing dense, more collimated flows from the youngest sources. The rovibrational H_2 1-0 S(1) line at $2.122 \mu\text{m}$ arises in regions with temperatures $\sim 2000\text{--}4000 \text{ K}$, and densities $10^3\text{--}10^5 \text{ cm}^{-3}$. Emission from this line indicates the presence of deeply embedded driving sources, and traces the youngest outflows.

Fig. 2 shows the integrated intensity map of CO $3 \rightarrow 2$ emission, in the velocity range -20 to 30 km s^{-1} (note all velocities are LSR unless otherwise stated). The brightest integrated emission (246 K km s^{-1}) is towards the cluster NGC 2264 C, while the brightest peak intensity (28 K) is towards the head of the Cone Nebula. Filaments can be seen extending south from NGC 2264 C, east and west from NGC 2264 D and north-west from the S Mon. S Mon is a

massive (17.8 M_{\odot}) young star, of spectral type O7V (Herrero et al. 1992), and the radiation pressure and wind from this star is likely to be heating and dynamically affecting nearby regions, such as the protostellar outflow source NGC 2264 G (Teixeira et al. 2008; Lada & Fich 1996). The two outflow lobes of NGC 2264 G can be seen to the north-east of S Mon. West of S Mon, and extending southwards, is a region of very weak emission, which we refer to as a cavity, surrounded by a ring or bubble of emission containing several SCUBA dust cores.

Dust pillars and cometary clouds, harbouring YSOs, are prevalent in *Spitzer* imaging of massive star forming regions (Smith et al. 2010), where the emission is dominated by strong PAH features. The Cone Nebula resembles one of these cometary regions in CO emission. The structure of this emission suggests that molecular gas is being ablated, possibly by the action of the NGC 2264 C cluster, exposing star forming cores. Red- and blue-shifted ^{12}CO emission and H_2 emission at the head of the Cone indicates ongoing star formation activity.

Fig. 3 shows a colour composite image of the H_2 1-0 S(1) and K-band images of NGC 2264³. Ellipses mark the Molecular Hydrogen emission-line Objects (MHOs) we have detected. Inset images show zoomed versions of these data towards two regions, the cluster NGC 2264 D and an isolated outflow to the south-east. H_2 line emission appears as turquoise in these images, which are shown in detail in Appendix Figs. 11 to 14. We detect 46 MHOs, of which 35 are new discoveries, and described in detail in the Appendix. We detect regions of multiple jets and bow shocks surrounding NGC 2264 C (extending further than seen by Wang et al. 2002), NGC 2264 D and NGC 2264 G (as seen by Reipurth et al. 2004). There are additional regions of jet activity to the east of NGC 2264 D, and in the south-east corner of the map. Towards the Fox Fur Nebula and the Cone Nebula, we see much larger-scale arcs and filaments in H_2 emission.

Representative CO spectra, and the intensity-weighted velocity map are shown in Fig. 4, highlighting the varying and complex velocity structure of this region. To the north, emission from the Fox Fur Nebula has narrow linewidths, and velocities $\geq 9 \text{ km s}^{-1}$. The star forming clusters, and NGC 2264 G have extended line wings due to outflow activity. The clustered regions of star formation are kinematically distinct, with different cloud velocities, as has been previously noted (Maury et al. 2009; Peretto et al. 2006). The Cone region, and NGC 2264 C, have velocities $\sim 7 \text{ km s}^{-1}$, while NGC 2264 D has velocities $\sim 5 \text{ km s}^{-1}$. Several regions show multiple velocity components, including the cavity south-east of S Mon, the Cone Nebula and NGC 2264 D.

Crutcher, Hartkopf & Giguere (1978) and Fűrész et al. (2006) identify distinct regions across NGC 2264 which are broadly in agreement with the velocity gradient and extent of the red, green and blue velocity regions in Fig. 4 respectively. Sung, Stauffer & Bessel (2009) identifies and assigns ages to distinct star forming clusters using *Spitzer* data. The region surrounding S Mon, including NGC 2264 G is aged at 3.1 Myr. The Cone Nebula is at a younger age, due to the number of embedded sources. Peretto, Henebelle & André (2007) calculates very young ages for the clusters NGC 2264 C and NGC 2264 D of ~ 0.1 Myr. We look at the regions of active star formation in more detail in the following section.

3 ACTIVE STAR FORMING REGIONS

The wide-field ^{12}CO 3 \rightarrow 2 and H_2 1-0 S(1) data can be used to provide a comprehensive quantitative analysis of the star formation activity across NGC 2264. Outflow and jet properties are expected to change as protostars evolve from the early accretion phase. The youngest objects, which are still accreting most of their final mass, are expected to have more powerful outflows, as measured from the CO momentum flux or jet luminosity (Caratti o Garatti et al. 2006; Arce & Sargent 2006; Bontemps et al. 1996). In the following analysis, we use CO 3 \rightarrow 2 to estimate the total outflowing mass, and the energy and momentum injected into the ambient cloud. We use H_2 1-0 S(1) to estimate the total H_2 luminosity in the jets, and place constraints on the impact of star formation activity on the ambient cloud.

For the emission in the outflow wings, we assume optically thin conditions, and calculate the total mass and energetics of molecular gas using emission from the ^{12}CO 3 \rightarrow 2 transition following Garden et al. (1991); Buckle et al. (2010). Maury et al. (2009) examined the opacity in the line wings of ^{12}CO using CO isotopologues towards the NGC 2264 C cluster, and found the emission to be optically thin outside of the central $\sim 10 \text{ km s}^{-1}$ of the line profile. For the outflow contribution at low velocities, the optically thin assumption may not be correct, and the masses are then lower limits. Since we make no correction for the inclination angle of the outflows, the values for momentum and kinetic energy are lower limits. We use an excitation temperature of $T_{\text{ex}} = 20 \text{ K}$ in order to aid comparisons with previously published work (e.g. Lada & Fich 1996). The data are thresholded at the 3σ level.

Due to the NGC 2264 velocity field (shown in Fig. 4), care needs to be taken in assigning velocity limits for the high velocity emission. We have taken the values from Peretto et al. (2006), who describe N_2H^+ observations, giving systemic velocities of 7.5 km s^{-1} for NGC 2264 C and 5.5 km s^{-1} for NGC 2264 D. For the high velocity material, we use the velocity intervals $\pm 5.0 \text{ km s}^{-1}$ to $\pm 20 \text{ km s}^{-1}$ either side of the systemic velocity for each cluster. For other regions, the sources are sufficiently isolated for an estimate of the systemic velocity to be made from ^{12}CO emission in areas adjacent to the molecular outflows. For NGC 2264 G, we use a systemic velocity of 5.0 km s^{-1} , with ranges up to $\pm 30 \text{ km s}^{-1}$ from the systemic velocity. Emission from ambient material covers the red lobe at low velocities, and so we use a lower velocity of 2 km s^{-1} for the red lobe, and -1 km s^{-1} for the blue lobe. For the protostar in the far south, IRAS2, we adopt a systemic velocity of 7.8 km s^{-1} , and velocity intervals of 2 to 10 km s^{-1} for the red-shifted emission, and -6 to -1 km s^{-1} for the blue-shifted emission.

We have extracted H_2 line emission fluxes from the H_2 plus continuum data after carrying out aperture photometry with background subtraction to calculate the calibrated integrated line flux. The H_2 plus continuum data is used rather than the continuum-subtracted data, since it does not add to the calibration uncertainties, and there are no deep negative components from an imperfect subtraction routine. Calibration was checked on stars in the field with known K-band magnitude, and is accurate at the 10% level.

The quadrupole transitions of H_2 (known as O, Q and S branches) are the main cooling mechanism for shock-excited jets detected in the near-IR. The rovibrational transitions arising in the near-IR, including the H_2 1-0 S(1) transition, can be used to estimate the total molecular hydrogen luminosity (L_{H_2}) of the flow. Younger flows are expected to have more powerful outflows, and higher values of L_{H_2} .

The total H_2 luminosity (L_{H_2}) can be calculated from the H_2 1-

³ K- and H_2 -band FITS data available from <http://www.jach.hawaii.edu/UKIRT/TAP/>

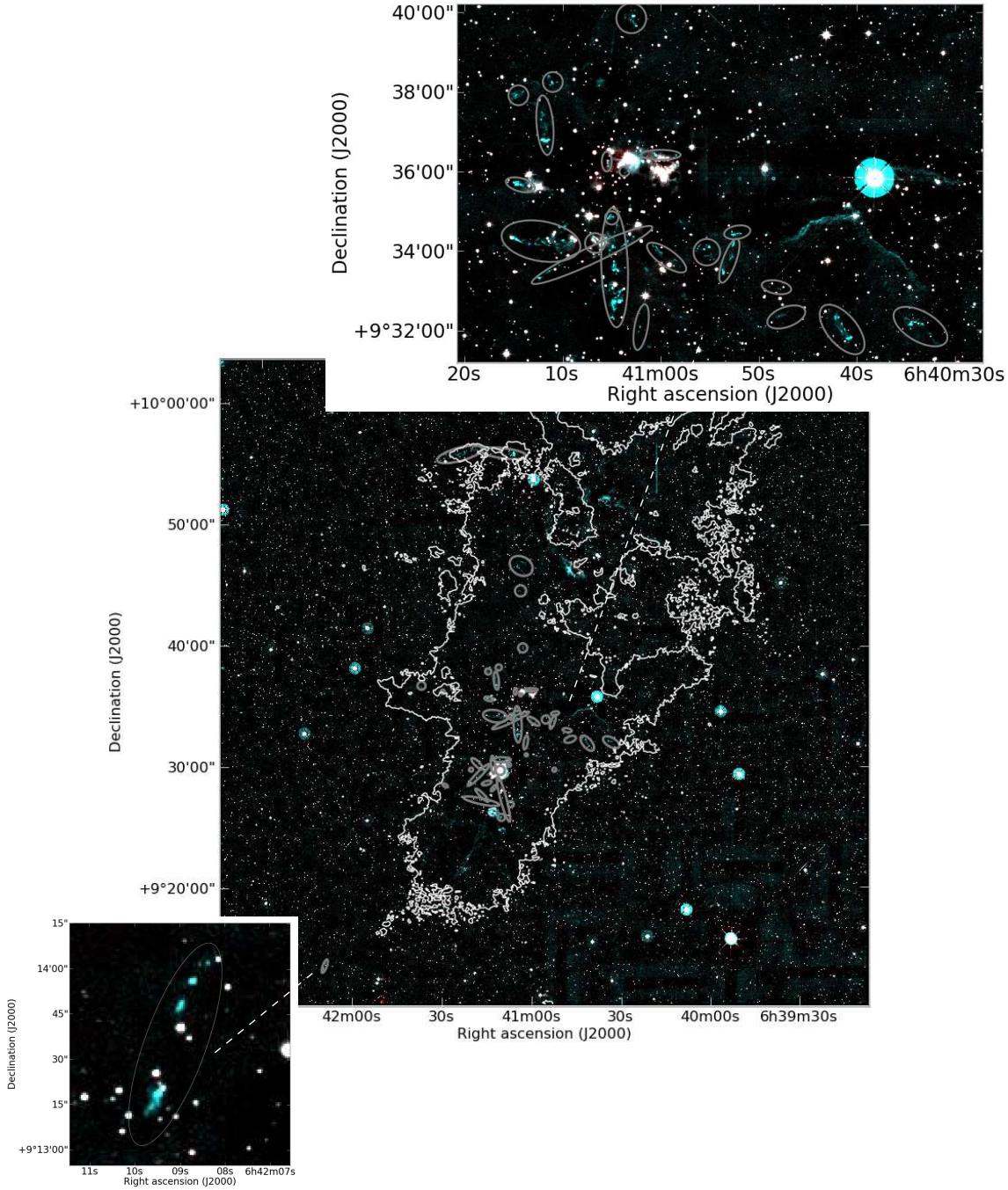


Figure 3. Colour composite image of the H₂ + continuum (blue and green) and K-band (red) data sets. Narrow-band H₂ line emission is seen in turquoise. The contour shows integrated CO emission at 15 K km s⁻¹. Ellipses mark the positions of MHOs we have detected, described further in the Appendix. Insets show zoomed images of two regions of newly detected MHOs, NGC 2264 D and a region in the south-east.

0 S(1) luminosity ($L_{H_{2,12}}$), with $L_{H_2} \sim 10 \times L_{H_{2,12}}$ (Caratti o Garatti et al. 2006), for typical H₂ jet temperatures between 1500 and 2500 K. If emission from the jet arises in regions at higher temperatures, this method will underestimate L_{H_2} by factors up to 2.5. L_{H_2} will also be underestimated by up to an order of magnitude in regions of high extinction ($A_v=25$). Caratti o Garatti et al. (2006) have used near-IR spectral line observations to calculate the temperature and extinction towards one of the flows in our dataset, NGC 2264 G. Their values of $T=2100-2800$ K, and $A_v=3-8$ mag suggest $L_{H_2} = 10 \times L_{H_{2,12}}$ is a reliable estimate of L_{H_2} for this region.

Table 1 shows the mass, momentum and kinetic energies calculated for the red- and blue-shifted CO 3 → 2 emission, and the H₂ luminosities, towards each region. Individual MHOs included for each region are described in the Appendix. For the whole cloud, $L_{H_2}=1.1 L_{\odot}$, although this is a lower limit, since we have not taken into account extinction. The masses are lower limits, since they are dependent upon temperature and opacity. If the high velocity emission is excited at temperatures >20 K, or the assumption of optically thin emission is not valid, then the masses will be increased.

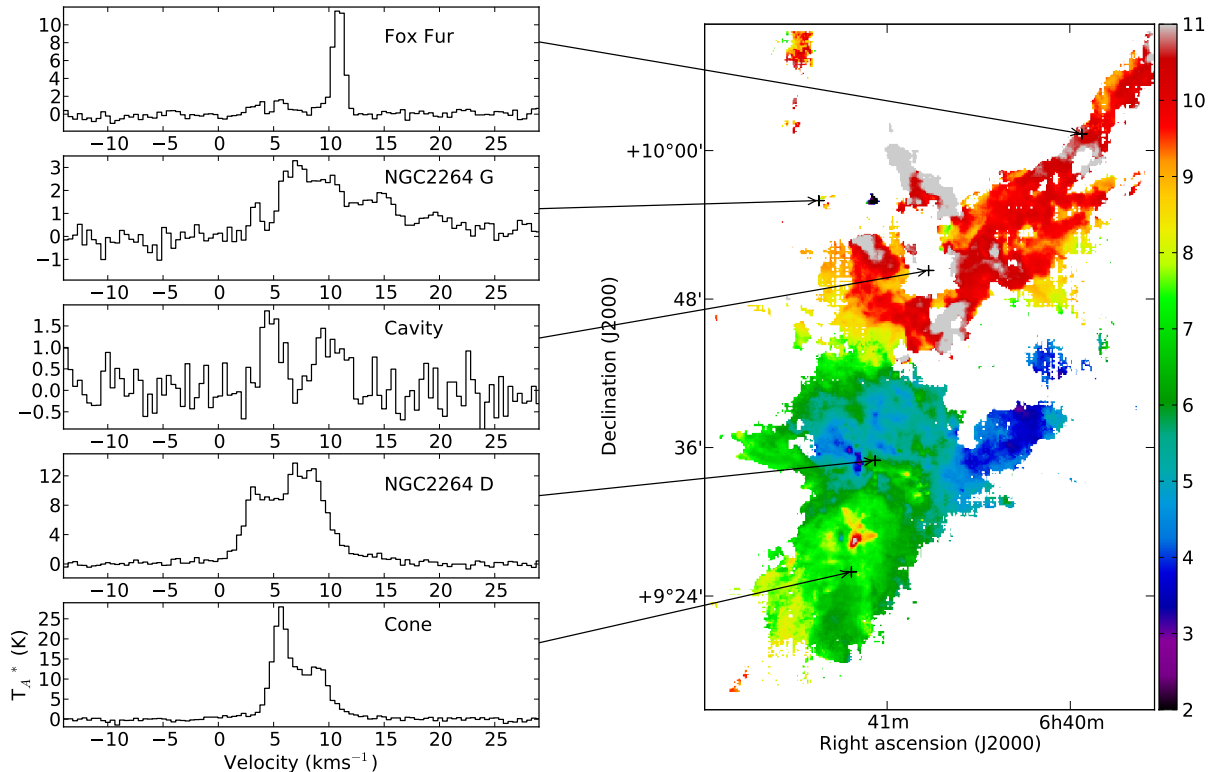


Figure 4. Spectra from individual pixels, from locations shown in the intensity-weighted velocity image, $\sum T_i v_i / \Delta v \sum T_i$, where $T_i, v_i, \Delta v$ are the intensity, velocity and velocity channel width respectively for each velocity channel, which is used to determine the velocity field. The intensity-weighted velocity data are thresholded to the $>3\sigma$ detection limit. The colour scale indicates the velocity field in units of km s^{-1} .

Additionally, it is not possible to entirely separate emission from outflowing gas from that of the ambient cloud.

Towards all of the active star forming regions, we find more mass, momentum and energy in the red-shifted material than in the blue-shifted material. Maury et al. (2009) has examined the individual flows in NGC 2264 C using CO and isotopic data, and also finds the red-shifted material to contain more mass and momentum. Asymmetry in molecular outflows is relatively common in low mass protostars, although no mechanism has so far been proposed for the brightening of the red-shifted lobe.

3.1 The NGC 2264 protoclusters

NGC 2264 D is a more massive cluster than NGC 2264 C, with more protostellar sources, more mass and energy, and covering a larger area. Within the uncertainties, both clusters have similar H_2 luminosities. Fig. 5 shows the red- and blue-shifted CO emission contoured over the H_2 image towards NGC 2264 C. The jets and outflows in the cluster can be seen extending past the Cone Nebula to the south. To the south-west of IRS1 is a red-shifted flow that contains the most high velocity gas, with line wings detectable out to $\sim 30 \text{ km s}^{-1}$. We have described in detail the individual H_2 objects and CO flows in the Appendix.

Peretto et al. (2006) identify 4 of the 12 NGC 2264 C cores as prestellar. As described in the Appendix, all four of these cores are spatially located within collimated red- and blue-shifted CO emission, and compact knots of H_2 emission. Additionally, 3 of the cores are coincident with *Spitzer* 24 μm sources. These data suggest

		CO 3 \rightarrow 2			H_2	
		Mass	Momentum	Energy	Area	L_{H_2}
		M_{\odot}	$M_{\odot} \text{ km s}^{-1}$	$\times 10^{36} \text{ J}$	pc^2	L_{\odot}
NGC 2264 C	red	1.70	14.6	146.0	1.7	0.41 ^a
	blue	1.38	11.1	105.3	1.9	
	all					
NGC 2264 D	red	2.63	21.8	212.9	3.4	0.37
	blue	1.72	15.3	159.0	2.5	
	all					
NGC 2264 G	red	0.55	7.1	111.2	0.8	0.25
	blue	0.36	4.1	61.1	0.4	
	all					
IRAS 2	red	0.08	0.3	1.4	0.3	0.01
	blue	0.04	0.1	0.3	0.4	
	all					

^a Emission from MHO1349 is excluded, since it can't be separated from the saturated continuum towards Allen's source.

Table 1. Outflow parameters for the NGC 2264 high velocity regions.

that these 4 cores are young Class 0/I protostars. Sung et al. (2009) classifies 17 24 μm sources as protostellar in NGC 2264 C.

Peretto et al. (2006) estimate the total gas mass in NGC 2264 C to be $1650 M_{\odot}$, compared to the $3 M_{\odot}$ we estimate to be entrained in the outflow. Although there are multiple energetic outflows in this cluster, only $\sim 0.2\%$ of the molecular gas has been entrained by outflows, or affected by star formation activity. This is a lower limit, since it is dependent upon the opacity.

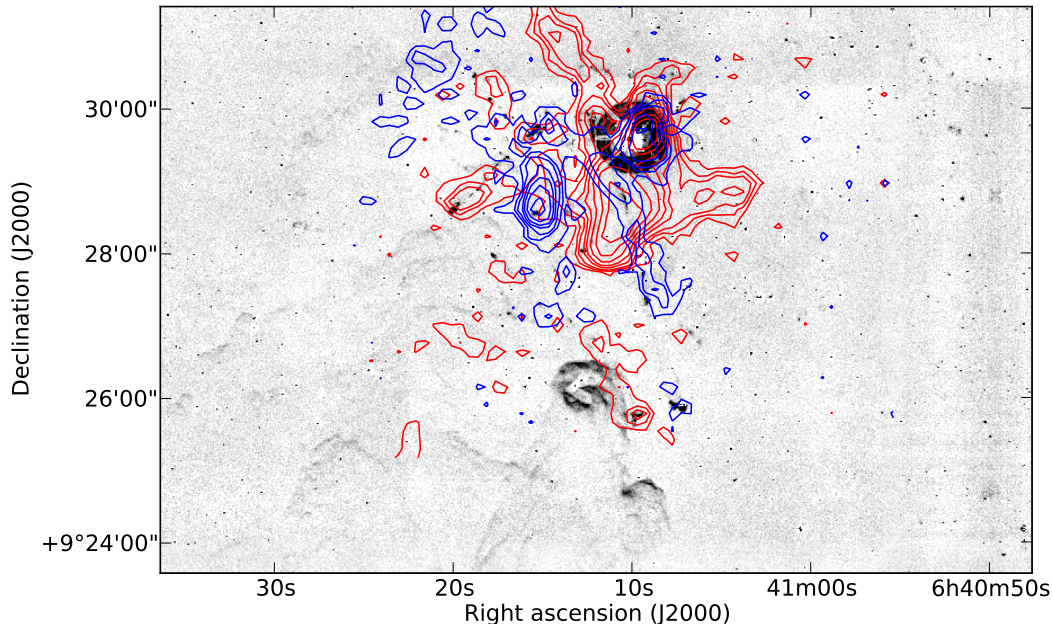


Figure 5. Red and blue shifted CO emission contoured over the H_2 continuum-subtracted greyscale image towards the NGC 2264 C cluster. Contours are at 3.9, 6.5, 9.1, 14.3, 19.5, 27.3, 37.7, 48.1 $K km s^{-1}$. Red-shifted emission extends from 12.2 to 30.9 $km s^{-1}$, and the blue-shifted from -17.8 to 2.1 $km s^{-1}$. The saturated source seen in the H_2 emission is Allen’s source (Allen 1972), IRS1.

Fig. 6 shows red- and blue-shifted CO emission contoured over the H_2 image towards NGC 2264 D. The cluster extends further westwards than previously observed, with the discovery of new jets and molecular outflows spatially adjacent to this cluster. The red-shifted emission contoured at the south-eastern edge of the map is from the NGC 2264 C cluster. The total gas mass is $1310 M_{\odot}$ in NGC 2264 D (Peretto et al. 2006), so the molecular outflows, entraining $5 M_{\odot}$, constitute a negligible fraction ($\sim 0.4\%$) of the cluster mass. Although this is a lower limit, this result implies that the large number of outflows are not affecting the bulk of molecular material.

Sung et al. (2009) classifies 44 sources as protostellar in NGC 2264 D. There are many overlapping CO outflows and H_2 jets, which we are unable to separate near the sources, making source identification difficult. Forbrich et al. (2010) identifies 3 embedded YSOs as candidate massive YSOs using PAH emission. One of these, SSB 11829 is co-incident with a ^{12}CO bipolar molecular outflow, and MHO 1385, a bright knot and extended west-facing bow shock, indicating the source is protostellar. A more detailed description of the individual H_2 objects and CO flows is given in the Appendix.

3.2 NGC 2264 G

The two outflow lobes of NGC 2264 G can be seen just to the northeast of S Mon in Fig. 2. The driving source (Teixeira et al. 2008; Gomez et al. 1994) has a mass, including the envelope, of 2–4 M_{\odot} . Teixeira et al. (2008) report *Spitzer* imaging of the protostellar jet, showing three changes in direction. Fig. 7 shows the red and blue contours for three different velocity ranges through the outflow lobes, overlaid on the H_2 emission from the protostellar jet. The CO emission from the molecular outflow follows the emission in the jet, including the changes in direction. There is a strong correlation between the structure of H_2 emission and high

velocity CO outflow lobes in the NGC 2264 G outflow. The extent of the H_2 emission matches the size of the CO lobes, and the H_2 intensity peaks are close to the peaks seen in the CO maps.

The total extent of the red outflow lobe is $\sim 280''$, or 1.1 pc (assuming 800 pc to NGC 2264), with the very high velocity gas ($>35 km s^{-1}$) extending further than the lower velocity gas. The low velocity emission ($6 km s^{-1}$) traces a cavity, while the high velocity emission ($40 km s^{-1}$) traces a collimated flow. The blue lobe has a small high velocity extension, and the total extent of the blue outflow lobe seen is $\sim 200''$, or 0.8 pc. These figures are in agreement with those derived from CO $2 \rightarrow 1$ observations (Lada & Fich 1996). The difference in the highest velocity spatial extent between the red and blue lobes we detect in CO $3 \rightarrow 2$ may be merely the amount of material available for entrainment in the two directions. The red lobe in Fig. 7(a) suggests a wide opening angle, with the H_2 emission (MHO 1359) associated with the northern edge of the flow. The clumpy structure seen very clearly in our new images of MHO 1359 could result from shocks fronts in the boundary layer between the flow and the ambient medium. The lack of H_2 emission along the southern edge of the flow lobe could be simply be due to a lower ambient density, suggesting a gradient in the ambient density that increases to the north across this region. Alternatively, Teixeira et al. (2008) propose a slowly precessing jet, plus additional deflection, to explain the structure. The broad red lobe we detect may suggest a density gradient, rather than a precessing jet. Table 1 gives the calculated outflow parameters for the NGC 2264 outflow. The total mass entrained in the outflow is $0.9 M_{\odot}$ with a momentum of $11 M_{\odot} km s^{-1}$. This is consistent with the mass and momentum found for the lower excitation CO $2 \rightarrow 1$ transition ($1 M_{\odot}$, $12 M_{\odot} km s^{-1}$, Lada & Fich 1996). The jet is bright, and has the highest L_{H_2} luminosity for an individual flow in this region.

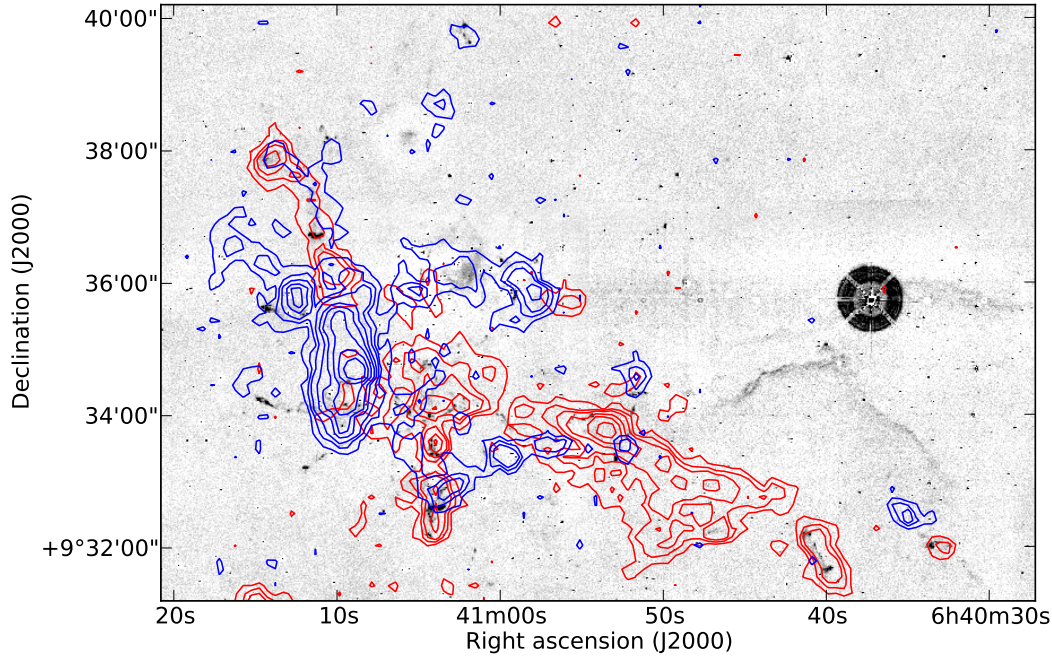


Figure 6. Red and blue shifted CO emission contoured over the H_2 continuum-subtracted greyscale image towards the NGC 2264 D cluster. Contours are at 3.9, 6.5, 9.1, 14.3, 19.5, 27.3, 37.7, 48.1 K km s^{-1} . Red-shifted emission extends from 11.1 to 25.5 km s^{-1} , and the blue-shifted from -18.5 to 1.0 km s^{-1} .

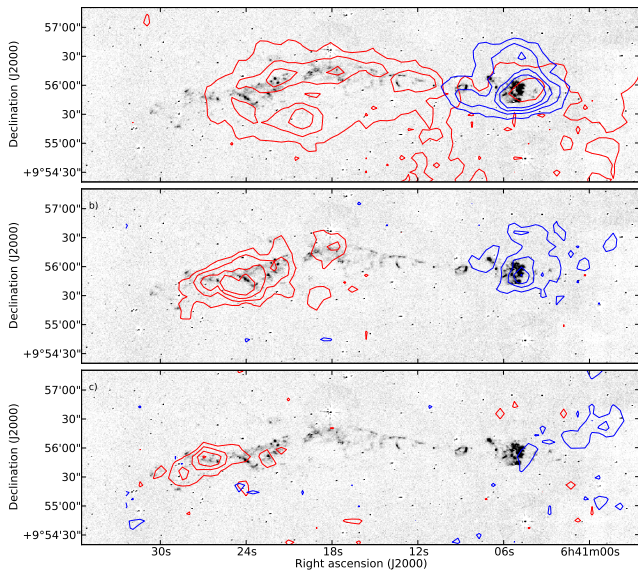


Figure 7. Red- and blue-shifted CO emission contours for three different velocity ranges towards NGC 2264, overlaid on the H_2 greyscale image. The red-shifted emission is associated with MHO 1359, the blue-shifted emission with MHO 1358. (a) Low-velocity gas at 6.0–8.0 km s^{-1} (red) and 1.0–3.0 km s^{-1} (blue). CO contours start at 2.5 K km s^{-1} , with steps of 2.5 K km s^{-1} . (b) Mid-velocity gas at 16.0–26.0 km s^{-1} (red) and -17.0–-7.0 (blue), contours as (a). (c) High-velocity gas at 29.0–39.0 km s^{-1} (red) and -30.0–-20.0 km s^{-1} (blue). CO contours start at 2.0 K km s^{-1} , with steps of 2.0 K km s^{-1} .

3.3 S Mon

S Mon is positioned in front of and travelling towards the NGC 2264 cloud (Tauber, Lis & Goldsmith 1993), affecting the region with an intense ionizing field. The emission surrounding

S Mon shows many filaments and arcs, although we do not detect any evidence from the presence of extended line wings, or the presence of H_2 knots, any protostellar outflow activity. The emission near S Mon is seen across a large velocity range, from 6.7 km s^{-1} to 13.5 km s^{-1} , and is characterized by relatively small linewidths, indicating that the complex kinematic structure is not due to protostellar outflow activity. At the highest red and blue velocities, the emission is very clumpy and fragmented. In the ring of emission (Fig. 2), a cluster of SCUBA cores to the north-west is associated with CO clumps at blue-shifted velocities, while the SCUBA cores to the south-east are associated with CO clumps at red-shifted velocities.

3.4 NGC 2264 IRAS-2

Fig. 8 shows outflow lobes associated with a source first detected by Margulis, Lada & Young (1989). This is a far-IR source with no optical counterpart and no previously detected outflow, designated as IRAS-2, with a luminosity of 6.7 L_{\odot} . Wolf-Chase, Wlaker & Lada (1995) detected an extended CS source at this position, but no outflow. Along with a weak CO molecular outflow, we also detect H_2 knots indicating protostellar jet activity, in MHO 3109 (Fig. 8).

The outflow candidate NGC 2264 A (Margulis, Lada & Snell 1988) is $\sim 400''$ east of IRAS-2. Although a red outflow lobe has previously been detected towards NGC 2264 A, we do not clearly detect the outflow lobe in CO $3 \rightarrow 2$ emission, or detect any H_2 emission.

3.5 IRAS 06396+0946

East of the main emission region, at the position $06^{\text{h}}42^{\text{m}}25^{\text{s}}.5 +09^{\circ}43'09''$ is a cometary-shaped feature, surrounded by several small, compact regions in ^{12}CO , which are blue-shifted to the north-west, and red-shifted to the south-east. The peak antenna tempera-

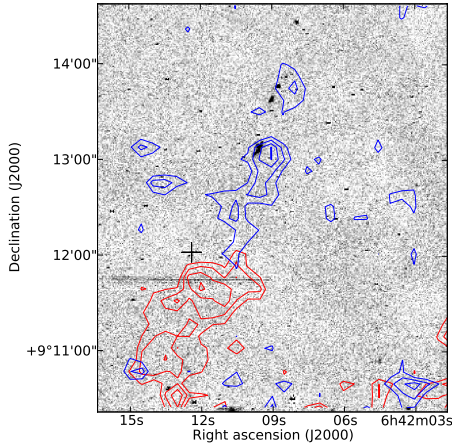


Figure 8. Red- and blue-shifted CO emission contours, overlaid on the H₂ greyscale image towards MHO 3109, shown as an ellipse. Red CO contours start at 3.0 K km s⁻¹ with 1.0 K km s⁻¹ steps, and blue contours start at 2.0 K km s⁻¹ with 0.8 K km s⁻¹ steps. A cross marks the position of the far-IR source IRAS2 (Margulis, Lada & Young 1989).

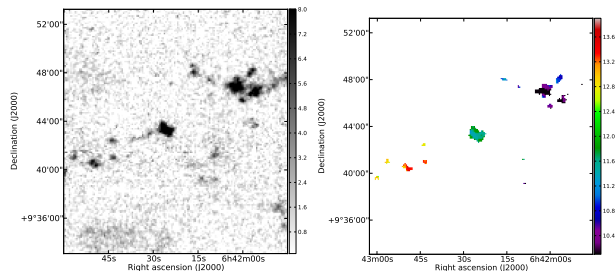


Figure 9. The isolated cometary feature east of the main NGC 2264 filament. Left: ¹²CO integrated intensity in greyscale. Right: The velocity field shown through the intensity-weighted velocity image. The velocity data has been thresholded at the 3 σ level for clarity.

ture is 10.8 K, and the lines are narrow, with FWHM ~ 1.0 km s⁻¹ from a Gaussian fit to the data. Fig. 9 shows the integrated intensity image of this region, in the velocity range 10.1 km s⁻¹ to 13.9 km s⁻¹ along with the intensity-weighted velocity image, which shows the velocity field. This is an intriguing structure, which could be associated with IRAS 06396+0946, although there is as yet no other published data on this region. The velocity field suggests an outflow or jet, although the morphology of the ¹²CO emission is more reminiscent of H₂ knots, such as those in the blue-shifted jet of NGC 2264 G, rather than the more linear or elliptical structures more commonly seen in CO. There is no H₂ emission associated with this object. The spatial alignment and velocity structure of this region may just be coincidental, however, with the emission arising in areas at different distances which are not related. More sensitive observations would be required to determine whether these emission regions are connected.

3.6 The NGC 2264 D filament

To the east of NGC 2264 D, there are two newly detected MHOs, MHO1378 and MHO1379, shown in the Appendix (Fig. 11b). The location of the MHOs and the velocity structure of the CO emission suggests that these MHOs may be associated with molecular outflows which are erupting from the dense gas in the cluster,

which contains several *Spitzer*-identified protostars (Sung et al. 2009). However, the line profiles do not have the line wings usually associated with molecular outflows. As the velocity increases from 1.0 km s⁻¹, two filaments extend eastwards from the bulk of the cluster, eventually overlapping and merging at velocities ~ 5.0 – 6.5 km s⁻¹, when the overall length is $\sim 11'$. At higher velocities, the filament becomes more pronounced, with additional internal structure that is very linear. The brightest regions are those furthest from the central cluster.

4 PRINCIPAL COMPONENT ANALYSIS

In order to undertake an analysis of the turbulent characteristics of NGC 2264, we have carried out a principal component analysis (PCA) on the ¹²CO data. The method is relatively robust against the effects of resolution and noise. The low-order components contain features that contribute most to the variance of the data, while higher-order components contain more subtle features within the spectral shapes.

We have implemented the technique described by Heyer & Schloerb (1997); Brunt & Heyer (2002a) and Brunt & Heyer (2002) who detail the methods in full. This technique transforms the original spectroscopic data cube (RA, Dec and velocity) into a set of orthogonal functions which are described by the principal components, l , ordered by decreasing variance of the data projected onto each orthogonal vector. The principal components consist of an eigenvector, tracing only the velocity structure, and an eigenimage, constructed from the projection of the data onto each of the eigenvectors. Each eigenimage therefore contains only spatial structure, mapping the size scales of differences in the line profiles traced by the eigenvectors. The principal components have characteristic length scales (L_l) determined from the eigenimage, and characteristic velocity scales (δv_l) determined from the eigenvectors. The eigenvectors and eigenimages of each principal component are coupled, so the physical dynamics can be determined from the characteristic scales. The data can be reconstructed from a linear combination of only the significant principal components, which account for most of the variance, or variability, in the data.

The technique provides an objective method of extracting the most significant components of the data for analysis, the challenge then being to interpret the results in a physically meaningful way. Brunt & Heyer (2002a) have carried out PCA on simulated data in order to provide empirical relations between the derived PCA results and the statistics of the original data, which we utilize in this analysis to aid the physical interpretation.

Brunt, Heyer & Mac Low (2009) used numerical magnetohydrodynamic models and molecular spectral line observations to show that the ratio of the characteristic length scales of the first two principal components (L_2/L_1) is related to the ratio of the turbulent driving scale to cloud size, (λ_D/L_D) for isotropically forced turbulence (see also Brunt 2003). Therefore, observational measures of L_2/L_1 can be used to estimate λ_D/L_D . For ratios > 0.2 , there is little sensitivity to the actual driving scale, and large-scale driving best describes the turbulent driving scale (Brunt et al. 2009).

4.1 Principal Components

Following Brunt (2003), we do not subtract the mean from the data, so that l_1 approximates the integrated intensity and mean line profile of the ¹²CO data. The scale of data values in the eigenvectors

l	Variance %	Cumulative Variance %	L_l pc	δv_l km s ⁻¹
1	74.15	74.15	7.5	6.3
2	20.86	95.01	2.6	2.5
3	3.16	98.18	1.3	1.7
4	0.73	98.90	0.6	1.3
5	0.51	99.41	0.6	0.8
6	0.21	99.63		
7	0.08	99.71		
8	0.05	99.76		
9	0.03	99.79		
10	0.02	99.82		

Table 2. Contribution of the first 10 principal components to the NGC 2264 CO data. Characteristic length and velocity scales for the 5 significant principal components are listed.

is not directly related to flux, but to the contribution of the principal component to each velocity channel. Large relative positive or negative values indicate that a principal component contributes significantly in that velocity channel. The eigenimages can be used as a diagnostic of how much spatial structure is associated with each eigenvector.

Table 2 lists the first 10 principal components, along with the variance of and the total cumulative variance for each component. The first five principal components contribute >99% of the variance, with l_1 accounting for 74% of the variation in the data. The largest values of L_l corresponds to the largest values of δv_l indicating that the largest velocity differences are distributed on the largest scales.

Fig. 10 shows the eigenimages and eigenvectors associated with the first 5 principal components. The black and white (positive and negative) regions in the eigenimages trace velocity fluctuations whose magnitude is indicated by the width of features in the eigenvectors. The first principal component, l_1 , as noted above, has an eigenimage which approximates the ¹²CO integrated intensity map. The centre velocity of the emission is 7.4 km s⁻¹, and it has a large an FWHM linewidth of 6.9 km s⁻¹, from a Gaussian fit to the eigenvector, which approximates the mean line profile of the ¹²CO data. l_2 shows a positive-negative dipole pattern that is characteristic of giant molecular clouds (Brunt et al. 2009), when the turbulence is driven on scales comparable to the cloud size. The lower velocity contributes mostly to spatial variations in the north, while the higher velocity contributes mostly to spatial variations in the south. This is consistent with the velocity field we determined for NGC 2264, discussed in Sec. 2.3. The positive velocity component of l_2 is at 5.4 km s⁻¹, with a linewidth of 4.2 km s⁻¹. This is spatially most closely associated with the emission from the star-forming clusters in the cloud, NGC 2264 C and NGC 2264 D. The negative velocity component of l_2 is at 10.4 km s⁻¹, and has a narrower linewidth of 2.6 km s⁻¹. This component is spatially most associated with emission from the region near S Mon, and the tip of the Cone. l_3 , with peaks at 4.0, 8.2 and 10.9 km s⁻¹, and linewidths of 2.9, 1.7 and 1.6 km s⁻¹, describes velocity and linewidth variations within the velocity components identified in l_1 and l_2 . All of the significant principal components also show an isolated, compact region of emission to the east of the main emission region, at the position associated with IRAS 06396+0946 (discussed in Sec. 3).

Further principal components describe successively smaller spatial variations in velocity and linewidths. By l_{20} , there is negligible emission in the eigenimages, and from these high-order prin-

cipal components, noise estimates can be made (Brunt & Heyer 2002).

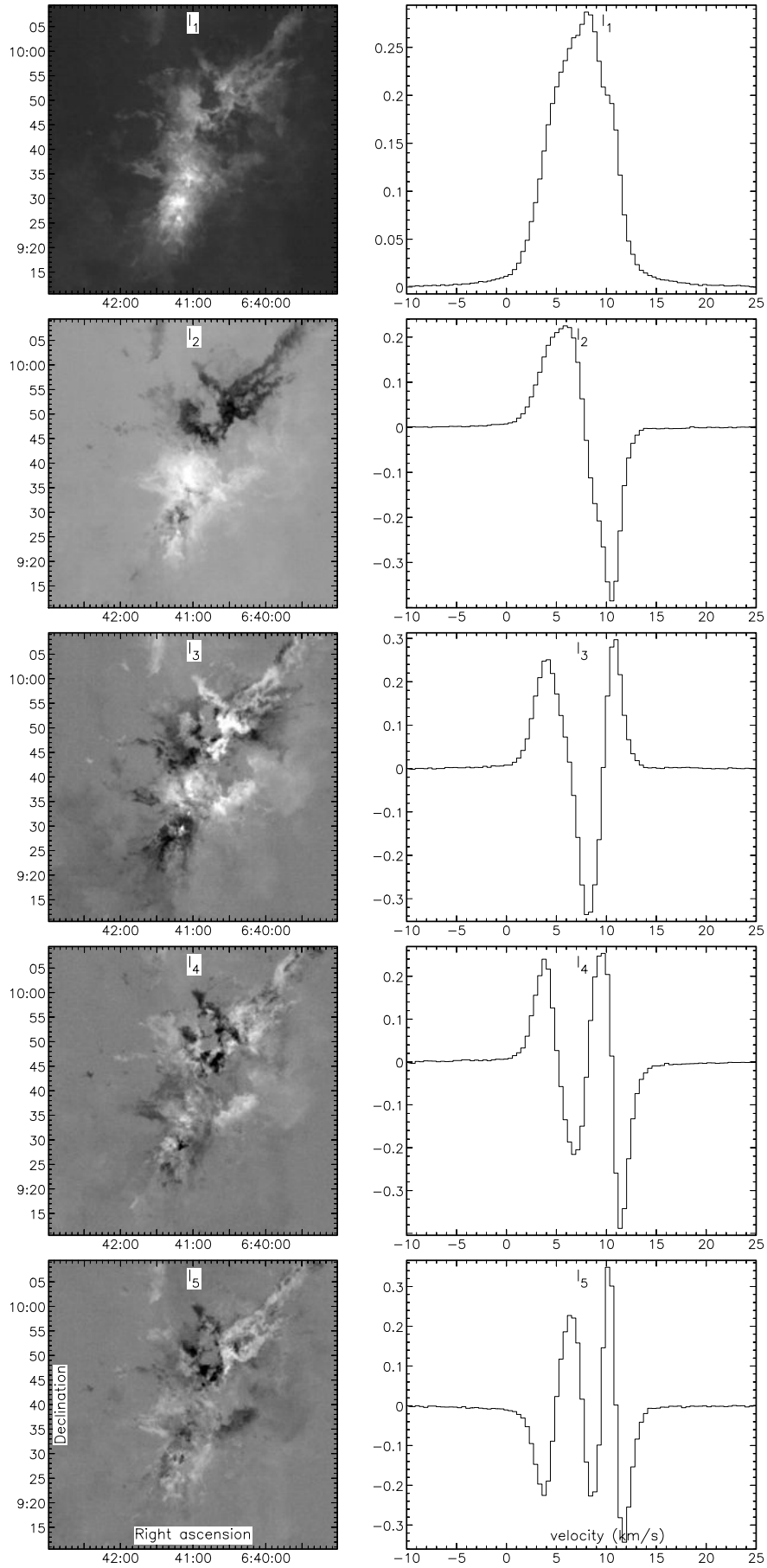
4.2 Characteristic Scales

Using results from the PCA decomposition, we can investigate the characteristic velocity variations and the spatial scales over which they occur. The characteristic scales are calculated using the normalized autocorrelation functions (ACFs) of each principal component, l , following Brunt & Heyer (2002a). The spatial scales are calculated using noise-subtracted, resolution-corrected ACFs. Given the limited number of spectral pixels, the characteristic velocity scale measurements are largely unaffected by instrumental noise. Instrumental noise and finite resolution effects are explained in detail by Brunt & Heyer (2002a), whose procedures we have implemented. The characteristic velocity and length scales (δv_l and L_l) are determined from the lag at which the normalized ACFs of the eigenvectors and eigenimages fall to e^{-1} , and are calculated following Heyer & Schloerb (1997).

The characteristic length scales L_l , and the characteristic velocity scales δv_l for the 5 significant principal components are listed in Table 2. Both the length and velocity scales decrease with increasing l . These scales can be visualized in the eigenimages and eigenvectors, where we can see, respectively, the spatial scale of variation, and the width of spectral features, decreasing as l increases. The assumption of a PCA analysis of molecular cloud spectral line data is that the decreasing size scales are reflecting a fundamental property of the kinematics of the gas within the cloud (Heyer & Schloerb 1997), from which turbulent driving scales (λ_D) can be determined. The longest flow we detect towards NGC 2264 is that of NGC 2264 G, at 280'', or 1.1 pc. Comparing this value with the L_l size scales suggests that the outflows we detect are contributing to the variance in the data at characteristic scales $< L_3$, and so are contributing $< 3\%$ to the variance in the data. They are not, therefore, contributing at the size scales necessary to be the main component driving turbulence. This is supported by our analysis in Sec. 3, where we found that $< 0.5\%$ of the cluster masses have been entrained within molecular outflows.

On the largest scales, the velocity variations are due to differences between components that make up the entire molecular cloud. The characteristic spatial scale of the first eigenimage, $L_1=7.5$ pc, therefore gives an estimate of the overall cloud size, L_D . The characteristic scale of the second eigenimage, $L_2=2.6$ pc, measures the size-scale over which the largest velocity variations occur in the data. $L_2=2.6$ pc can therefore be associated with the turbulent driving scale.

Carroll, Frank & Blackman (2010) have examined the use of PCA in simulations of outflow driven turbulence, isotropically forced turbulence, and a combination of both. They find that the ratio of characteristic length scales l_2/l_1 correctly identifies the largest driving scale in all three types of simulations, but suggest the scales derived from PCA are measuring the largest scale of coherent motion, which is not necessarily the turbulent driving scale. As noted by Carroll et al. (2010), this distinction is important in clouds where outflows are present within an external cascade, or where there are large-scale coherent motions due to angular momentum conserving collapse. In our PCA analysis, the principal components describe a large-scale velocity field across the cloud, with contributions from high velocity outflow emission. As shown in Fig. 4, the velocity field of NGC 2264 shows little evidence for large-scale coherent motions. There is no indication of a rotation axis for the region as a whole.



We follow Brunt et al. (2009) and use the ratio of the characteristics length scales, l_2/l_1 , to estimate the turbulent driving scale. From the ratio of the spatial scales of the first two eigenimages, we derive a fractional driving scale of 0.35, indicating large-scale driving. Combined with the characteristic scale $L_2=2.6$ pc associated with the turbulent driving scale, and our analysis in Sec. 3, these data indicate that protostellar outflow activity in NGC 2264 is not the dominant component of turbulence, even though it is a young and energetic star forming region.

4.3 Size-linewidth correlation

Larson (1981) developed an empirical relation between the linewidth ΔV and cloud size R , with $\Delta V \propto R^\alpha$, and $\alpha=0.5$. This power-law relation is similar to that expected from studies of turbulence, where values of α can range from $\alpha = 1/3$ for the incompressible energy cascade to $\alpha = 1/2$ for a shock-dominated turbulent fluid (McKee & Ostriker 2007, and references therein). The equivalent PCA velocity statistic α is obtained from the set of significant $\delta v_l - L_l$ pairs which are larger than the resolution limits. These form the power-law relationship $\delta v \propto L^\alpha$. Brunt (2003) compared observations to simulations, and obtained values of α from 0.5 to 0.8.

Brunt et al. (2003) relate the exponent of the characteristic velocity and length scale relation, α , to the scaling properties of the intrinsic velocity field. Roman-Duval et al. (2011) derive a PCA calibration for the exponent of the turbulent velocity spectrum $E(k) \propto k^{-\beta_v}$, finding $\beta_v = 0.2 \pm 0.05 + (2.99 \pm 0.09)\alpha$. Values of $\beta = 5/3$ are expected for the incompressible energy cascade model (Elmegreen & Scale 2007, and references therein). Roman-Duval et al. (2011) applied their results to a sample of 367 molecular clouds, finding $\langle \alpha \rangle = 0.61 \pm 0.2$, and $\langle \beta \rangle = 2.06 \pm 0.6$.

We calculate $\alpha = 0.74 \pm 0.08$ and $\beta = 2.4$ from our PCA analysis. The value of α is larger than that expected from a classic linewidth-size relationship (Larson 1981) in giant molecular clouds, but is consistent with measurements towards the NGC 2264 C region (Maury et al. 2009) using observations of ^{13}CO . The size-linewidth correlation is thought to depend upon the mean surface density of the cloud (Heyer et al. 2009), and so α values will be higher in regions of high surface density. NGC 2264 has a mean surface density >10 times that assumed for the classic linewidth-size relation (Maury et al. 2009). $\alpha = 0.74$ is consistent with values found in high mass star forming regions such as the Rosette molecular cloud (Heyer, Williams & Brunt 2006).

The β value of 2.4, giving $E(k) \propto k^{-2.4}$, is larger than values expected for Kolmogorov-type turbulence, but is similar to values found using ^{12}CO towards Perseus (Sun et al. 2006), where values were higher in active star forming regions than in dark clouds. A steep energy spectrum is consistent with the energetic star formation activity of NGC 2264.

5 SUMMARY

We have presented wide-field spectral imaging observations in ^{12}CO 3 \rightarrow 2 and wide-field high resolution imaging observations in H_2 1-0 S(1) towards NGC 2264. These observations, covering nearly 1 square degree, offer a detailed view of the star formation activity taking place in this clustered environment. We find that

(i) Protostellar outflow activity in NGC 2264 does not occur on

large enough scales to drive the turbulence. The largest flows extend to ~ 1 pc, while a PCA analysis suggests that turbulence is driven on scales larger than 2.6 pc.

(ii) Only a small fraction, $<0.5\%$, of the cluster gas mass in NGC 2264 C and NGC 2264 D, has been swept up to high velocities through protostellar outflow activity. The outflow activity is not having a sufficient impact on the cloud to be the dominant source of turbulence.

(iii) We detect 46 molecular jets and knots in H_2 , 35 of which are new detections. Based on the new H_2 data, NGC 2264 C and NGC 2264 D extend to a larger spatial extent than previously determined.

(iv) NGC 2264 D contains a larger mass of gas at higher velocities, and also more energy and momentum than NGC 2264 C.

(v) Due to the presence of spatially distinct red- and blue-shifted CO emission, and H_2 emission in the form of jets or bow shocks, we characterize 4 cores in NGC 2264 C as protostellar that were previously identified as prestellar.

(vi) Of three massive YSO candidates in the NGC 2264 D cluster, we detect a bipolar molecular outflow and H_2 jet towards SSB 11829.

The large number of protostars, jets and outflows in the NGC 2264 region, and their small separations, require very high resolution observations in order to isolate the flows and identify driving sources. This will be possible in future observational studies with the resolution and sensitivity offered by ALMA.

6 ACKNOWLEDGMENTS

We thank the referee for very useful comments which have improved the paper. The United Kingdom Infrared Telescope is operated by the Joint Astronomy Centre on behalf of the Science and Technology Facilities Council of the U.K. The infrared data reported here were obtained as part of the UKIRT Service Programme, Programme I.D. U/SERV/1764. The James Clerk Maxwell Telescope is operated by The Joint Astronomy Centre on behalf of the Science and Technology Facilities Council of the United Kingdom, the Netherlands Organisation for Scientific Research, and the National Research Council of Canada. The CO data reported here were obtained as part of Programme I.D. M07BU09. This research used the facilities of the Canadian Astronomy Data Centre operated by the National Research Council of Canada with the support of the Canadian Space Agency. This paper made use of data products from the JCMT Science Archive (JSA) project. The JSA is a collaboration between the James Clerk Maxwell Telescope (JCMT) and the Canadian Astronomy Data Center (CADC).

REFERENCES

- Adams M.T., Strom K.M., Strom S.E., 1983, ApJS, 53, 893
- Allen D.A., 1972, ApJL, 172, 55
- Arce H.G., Sargent A.I., 2006, ApJ, 646, 1070
- Baxter E.J., Covey K.R. Muench A.A., Fűrész G. Rebull L., Szentgyorgyi A.H., 2009, AJ, 138, 963
- Bontemps S., André P., Terebey S., Cabrit S., 1996, A&A, 311, 858
- Buckle J.V., Hills R.E., Smith H. et al., 2009, MNRAS, 399, 1026
- Buckle J.V., Curtis E.I., Roberts J.F. et al., 2010, MNRAS, 401, 204
- Brunt C.M., Heyer M.H., Mac Low M.-M., 2009, A&A, 504, 883

- Brunt C.M., 2003, *ApJ*, 583, 280
- Brunt C.M., Heyer M.H., Vázquez-Semadeni E., Pichardo B., 2003, *ApJ*, 595, 824
- Brunt C.M., Heyer M.H., 2002a, *ApJ*, 566, 276
- Brunt C.M., Heyer M.H., 2002, *ApJ*, 566, 289
- Caratti o Garatti A., Giannini T., Nisini B., Lorenzetti D., 2006, *A&A*, 449, 1077
- Carroll J.J., Frank A., Blackman E.G., 2010, *ApJ*, 722, 145
- Casali M., Adamson A., Alves de Oliveira C., et al., 2007, *A&A*, 467, 777
- Currie, M.J., Draper, P.W., Berry D.S., Jenness T., Cavanagh B., Economou F., 2008, in Argyle R.W., Bunclark P.S., Lewis J.R., eds, *ASP Conf. Ser. Vol. 394, Astron. Data Analysis Software and Systems* p. 650
- Crutcher R.M., Hartkopf W.I., Giguere P.T., 1978, *ApJ*, 226, 839
- Dahm S.E., 2009, in Reipurth B., ed, *Handbook of Star Forming Regions Vol. I: The Northern Sky*, p. 966
- Dahm S.E., Simon T. 2005, *AJ*, 129, 829
- Davis C.J., Eislöffel J., 1995, *A&A*, 300, 851
- Davis C.J., Froebrich D., Stanke T., Megeath S.T., Adamson A. et al., 2009, *A&A*, 496, 153.
- Di Francesco J., Johnstone D., Kirk H., MacKenzie T., Ledwosinska E., 2008, *ApJS*, 175, 277
- Elmegreen B.G., Scalo J., 2004, *ARAA*, 42, 211
- Forbrich J., Tappe A., Robitaille T., Muench A.A., Teixeira P.S., et al., 2010, *ApJ*, 716, 1453
- Fűrész G., Hartmann L.W., Szentgyorgyi A.H., et al., 2006, *ApJ*, 648, 1090
- Garden R. P., Hayashi M., Hasegawa T., Gatley I., Kaifu N., 1991, *ApJ*, 374, 540
- Gomez J.F., Curiel S. Torrelles J.M., Rodriguez L.F., Anglada G., Girart J.M., 1994, *ApJ*, 436, 749
- Hedden A.S., Walker C.K., Groppi C.E., Butner H.M., 2006, *ApJ*, 645, 345
- Herrero A., Kudritzki R.P., Vilchez J.M., Kunze D., Butler K., Haser S., 1992, *A&A*, 261, 209
- Heyer M.H., Krawczyk C., Duval J., Jackson J.M., 2009. *ApJ*, 699, 1092
- Heyer M.H., Williams J.P., Brunt C.M., 2006, *ApJ*, 643, 956
- Heyer M.H., Schloerb F.P., 1997, *ApJ* 475, 173
- Jenness T., Cavanagh B., Economou F., Berry D.S., 2008, in Argyle R.W., Bunclark P.S., Lewis J.R., eds, *ASP Conf. Ser. Vol. 394, Astron. Data Analysis Software and Systems* p. 565
- Kutner M.L., Ulich B.L., 1981, *ApJ*, 250, 341
- Lada C.J., Fich M., 1996, *ApJ*, 459, 638
- Larson R.B., 1981, *MNRAS*, 194, 809
- Margulis M., Lada C.J., Snell R.L., 1988, *ApJ*, 333, 316
- Margulis M., Lada C.J., Young E.T., 1989, *ApJ*, 345, 906
- Maury A.J., André P., Li Z.-Y., 2009, *A&A*, 499, 175
- McKee C.F., Ostriker E.C., 2007, *ARAA*, 45, 565
- Peretto N., Hennebelle P., André P. 2007, *A&A*, 464, 983
- Peretto N., André P., Belloche A., 2006, *A&A*, 445, 979
- Reipurth B., Yu K.C., Moriarty-Schieven G., Bally J., ASPIN C., Heathcote S., 2004, *AJ*, 127, 1069
- Roman-Duval J., Federrath C., Brunt C., Heyer M., Jackson J., Klessen R., 2011, *ApJ*, 740, 120
- Tauber J.A., Lis D.C., Goldsmith P.F., 1993, *ApJ*, 403, 202
- Teixeira P.S., McCoe C., Fich M., Lada C.J. 2008, *MNRAS*, 384, 71
- Teixeira P.S., Lada C.J., Young E.T. et al., 2006, *ApJL*, 636, 45
- Schreyer K., Helmich, F.P., van Dishoeck E.F., Henning Th., 1997, *A&A*, 326, 347
- Smith N., Povich M.S., Whitney B.A., Churchwell E., Babler B.L., et al., 2010, *MNRAS*, 406, 952
- Sun K., Kramer C., Ossenkopf V., Bensch F., Stutzki J., Miller M., 2006, *A&A*, 541, 539
- Sung H., Stauffer J.R., Bessell A.S., 2009, *AJ*, 138, 1116
- Thompson R.I., Corbin M.R., Young E., Schneider G., 1998, *ApJL*, 492, 177
- Ward-Thompson D., Zylka R., Mezger P.G., Sievers A.W., 2000, *A&A*, 355, 1122
- Wang H., Yang J., Wang M., Yan J., 2002, *A&A*, 389, 1015
- Williams J.P., Garland C.A., 2002, *ApJ*, 568, 259
- Wolf-chase G., Moriarty-Schieven G., Fich M., Barsony M., 2003, *MNRAS*, 344, 809
- Wolf-Chase G., Walker C.K., Lada C.J., 1995, *ApJ*, 442, 197
- Young E.T., Teixeira P.S., Lada C.J., et al, 2006, *ApJ*, 642, 972
- Zinnecker H., Yorke H.W., 2007, *ARA&A*, 45, 481

7 APPENDIX A

7.1 Molecular Hydrogen emission-line Objects

Table 3 lists the 46 Molecular Hydrogen emission-line Objects (MHOs) identified in this work. Of these, MHO 1375-1399 and MHO 3100-3109 are new discoveries. Fig. 11–12 show the H₂ emission maps of the MHOs listed in Table 3. H₂ emission maps of NGC 2264 C and NGC 2264 D are shown in the next section to aid visualization when discussing the clusters.

7.2 The protostellar content of NGC 2264 C

NGC 2264 C is associated with IRS1, or Allen’s source, an early B star discovered by Allen (1972), who estimated extinction towards the source as $A_V \sim 26$. The group of prestellar cores and protostars to the south are known as the cluster NGC 2264 C (Margulis, Lada & Snell 1988; Peretto et al. 2006), where star formation has probably been triggered by activity from IRS1 (Thompson et al. 1998; Williams & Garland 2002). The cores are forming several intermediate/high mass stars (Peretto et al. 2006; Ward-Thompson et al. 2000), with core masses of 1–50 M_⊙ measured from submillimetre observations. Previous studies with a variety of molecular lines have pointed to the complex velocity field in this cluster, with IRS1 associated with velocities between 8–10 km s⁻¹, surrounded by several sub-clouds with velocities of 5.5–7 km s⁻¹ (Schreyer et al 1997). The emission also extends to the west, with no obvious driving source, or any H₂ counterparts. IRS1 itself drives a tightly peaked, overlapping molecular outflow. There are several submm and Class I cores clustered in the region of the IRS1 source that could be driving these energetic flows.

Peretto et al. (2006) identifies 4 prestellar cores, and 8 protostellar cores towards the clump near NGC 2264 C, from observations of the 1.2 mm dust continuum, and the optically thin tracer N₂H⁺. Fig. 13 shows the CO molecular outflows and H₂ jets, marked with the positions of the pre- and protostellar cores, adopting the labelling scheme of Peretto et al. (2006, 2007), and labelling the cores CMM1–CMM13. Of these, we detect possible outflows towards all of the prestellar cores, based on the presence of spatially distinct red- and blue-shifted emission, and H₂ emission in the form of jets or bow-shocks. The presence of H₂ jets indicates that these cores are young Class 0 sources. The cores CMM6, CMM7 and CMM8 are located to the south of NGC 2264 C, and Peretto et al. (2006) indicates that they are not associated with

Table 3. Molecular Hydrogen emission line Objects (MHOs) in NGC 2264*.

Object ^a	RA (2000.0)	Dec (2000.0)	Assoc. ^b HH Object	Note
MHO 1349	06 41 10.5	+09 29 47		Emission associated with NGC 2264 C
MHO 1350	06 41 09.9	+09 28 14		Knotty jet extending to south of NGC 2264 C/eclipsing TTS KH 15D
MHO 1351	06 41 12.2	+09 29 50		Arc in NGC 2264 C region; possibly associated with MHO 1350
MHO 1352	06 41 15.3	+09 29 44		Collimated jet 1-2 arcmin ESE of NGC 2264 C
MHO 1353	06 41 17.9	+09 30 08		Chain of knots in the NGC 2264 C region
MHO 1354	06 41 15.3	+09 28 34		Compact knot in the NGC 2264 C region
MHO 1355	06 41 17.7	+09 27 59		Small knot in the NGC 2264 C region
MHO 1356	06 41 12.7	+09 28 03		Compact feature in the NGC 2264 C region
MHO 1357	06 41 16.8	+09 27 10		Small, faint knot in the NGC 2264 C region
MHO 1358	06 41 05.0	+09 55 50		Complex group of knots associated with bipolar outflow NGC 2264 G
MHO 1359	06 41 23.0	+09 55 45		Faint arcs and filaments associated with bipolar outflow NGC 2264 G
MHO 1375	06 41 04.2	+09 46 35	HH 125	Knots and extended bows ~7' south of S Mon in NGC 2264
MHO 1376	06 41 03.7	+09 44 32	HH 225	Knots and faint emission ~7' south of MHO 1375 (unrelated)
MHO 1377	06 41 02.2	+09 39 51	HH 226	Two compact knots to the north of a cluster of outflows near NGC 2264 D
MHO 1378	06 41 36.5	+09 36 31		Compact knot to the west of the NGC 2264 D cluster
MHO 1379	06 41 29.3	+09 36 08		Faint feature to the west of the NGC 2264 D cluster
MHO 1380	06 41 14.3	+09 37 50		Faint knots and emission in NE corner of the NGC 2264 D cluster
MHO 1381	06 41 10.6	+09 38 10		Compact knot plus diffuse emission in NE corner of the NGC 2264 D cluster
MHO 1382	06 41 11.3	+09 36 42		Bright, knotty arc plus diffuse emission in the NGC 2264 D cluster
MHO 1383	06 41 04.8	+09 36 07		Faint emission in the NGC 2264 D cluster
MHO 1384	06 41 02.7	+09 35 55		Faint emission in the NGC 2264 D cluster
MHO 1385	06 41 00.0	+09 36 19		Bright knot and extended west-facing bow shock in
MHO 1386	06 41 14.3	+09 35 35		Bright, knot bows moving north-eastward from the NGC 2264 D region
MHO 1387	06 41 14.2	+09 34 10		Arcs and filaments in flow moving eastward from the NGC 2264 D region
MHO 1388	06 41 05.6	+09 34 02		Compact knots and fingers off emission in the NGC 2264 D cluster
MHO 1389	06 41 04.8	+09 34 44		Knots and emission in the NGC 2264 D region
MHO 1390	06 41 06.2	+09 33 44		Extended, collimated outflow in the NGC 2264 D cluster
MHO 1391	06 41 04.2	+09 33 32		Bright, extended outflow that crosses MHO 1390 in the NGC 2264 D region
MHO 1392	06 40 59.4	+09 33 50		Faint fingers of emission extending to the south-west in NGC 2264 D
MHO 1393	06 40 54.9	+09 33 55		Group of knots and arcs in the NGC 2264 D region
MHO 1394	06 40 51.9	+09 34 18		Small group of knots; possibly associated with the MHO 1395 jet
MHO 1395	06 40 52.9	+09 33 19		Bright bow shock and knotty jet to the west of the NGC 2264 D cluster
MHO 1396	06 41 01.5	+09 31 57	HH 581	Very faint outflow in the NGC 2264 D region
MHO 1397	06 40 48.2	+09 32 58		Knot and faint emission a few arcmins to west of the NGC 2264 D cluster
MHO 1398	06 40 47.2	+09 32 13		Knot and faint emission a few arcmins to west of the NGC 2264 D region
MHO 1399	06 40 39.8	+09 31 41		Arcs plus diffuse emission in feature to west of the NGC 2264 D region
MHO 3100	06 40 33.6	+09 32 00		Small group of knots plus faint emission ~1.5' west of MHO 1399
MHO 3101	06 40 52.3	+09 29 43		Compact feature to south of the NGC 2264 D cluster
MHO 3102	06 41 01.4	+09 30 56		Compact feature to south-west of the NGC 2264 D cluster
MHO 3103	06 41 10.2	+09 30 27		Curving chain of knots/outflow ~1' north of NGC 2264 C
MHO 3104	06 41 19.9	+09 29 41		Knot plus faint fingers of emission ~2.5' east of NGC 2264 C
MHO 3105	06 41 28.8	+09 28 24		Diffuse arcs of emission ~4.5' ESE of NGC 2264 C
MHO 3106	06 41 07.4	+09 30 04		Two compact knots ~1' north-east of NGC 2264 C
MHO 3107	06 41 06.8	+09 26 54		Knot plus faint emission ~3' south of NGC 2264 C
MHO 3108	06 41 09.6	+09 25 45		Bright knot and arc of emission ~4' south of NGC 2264 C
MHO 3109	06 42 09.5	+09 13 09		Chain of half-a-dozen knots in a flow in the south of NGC 2264

^a For discovery images of MHO 1349-1357 see Wang et al. (2002); MHO 1358/1359 was first imaged in H₂ by Davis & Eisloffel (1995). MHO 1375-1399 and MHO 3100-3109 are new discoveries.

^b Associated HH object, if any (see Reipurth et al. 2004, for details).

* For a complete list and individual images of MHOs, see: <http://www.jach.hawaii.edu/UKIRT/MHCat/>

any MSX or 2MASS sources, or any H₂ jets. In Fig. 13, CMM7 is associated with a relatively bright *Spitzer* 24 μ m source, while CMM6 is spatially coincident with a faint 24 μ m source, and all three are associated with red- and blue-shifted elongated emission which could be arising in protostellar outflows. In addition, CMM9, the northern-most source to the east of NGC 2264 C also appears

to have a molecular outflow, and be associated with a weak 24 μ m source. We propose that these are all, in fact, protostellar sources, induced by the activity of NGC 2264 C. Table. 4 summarizes the CO outflows and MHOs we have been able to associate with a driving source, and the lengths of the flows, measured from either the H₂ emission, or from CO red- or blue-shifted emission.

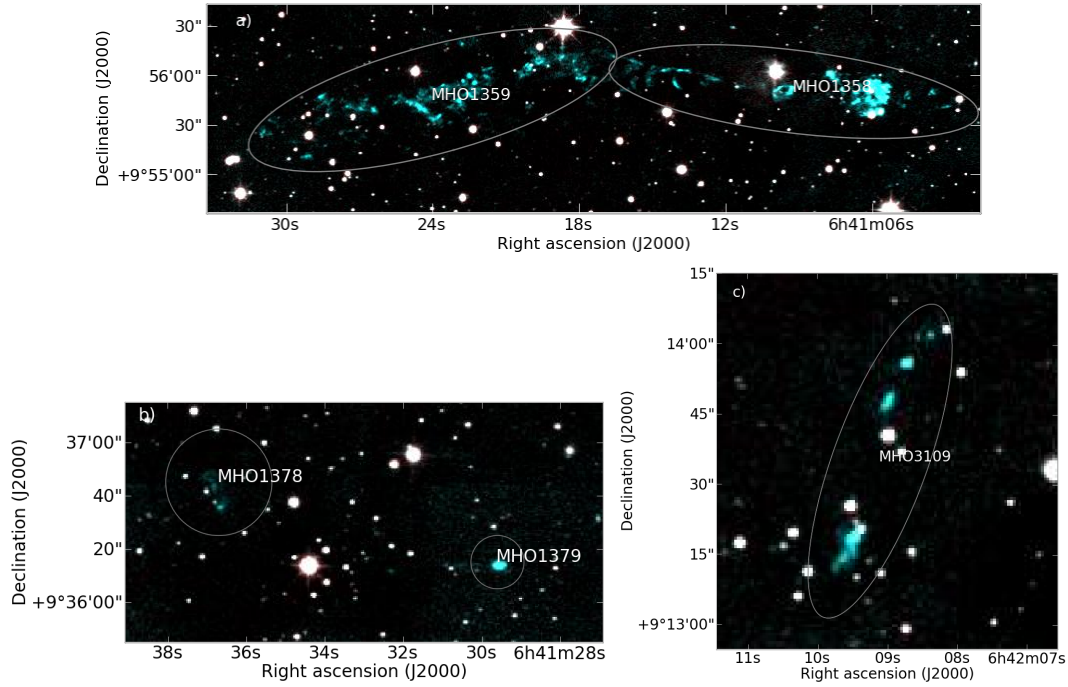


Figure 11. H₂ colour composite images (as Fig. 3) of a) NGC 2264 G. b) The NGC 2264 D filament. c) NGC 2264 IRAS2

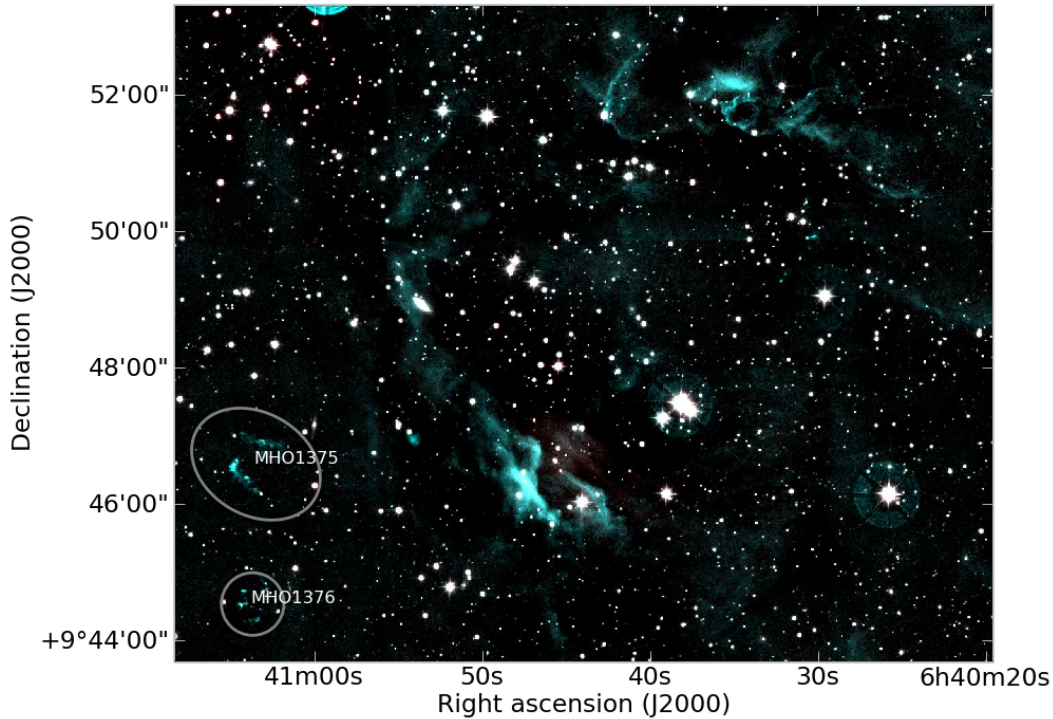


Figure 12. H₂ colour composite image of S Mon, as Fig. 3.

CMM1 drives a double-sided H₂ jet, MHO1352, and has a clearly defined red outflow lobe. The blue outflow lobe is driving towards the centre of the cluster, directly towards CMM9, and so can only be seen as a spatial extension in the blue shifted emission, aligned along the H₂ jet direction.

CMM2 is at the base of a chain of H₂ knots and fingers,

MHO1304, that is also associated with weak blue-shifted emission. We are not able to associate any red-shifted emission from this source due to the strong outflow lobes at the centre of the cluster. A *Spitzer* 24 μm identified protostar, 14214 (Sung et al. 2009) is 8'' north of CMM2.

MHO1356 is associated with a large red-shifted outflow lobe.

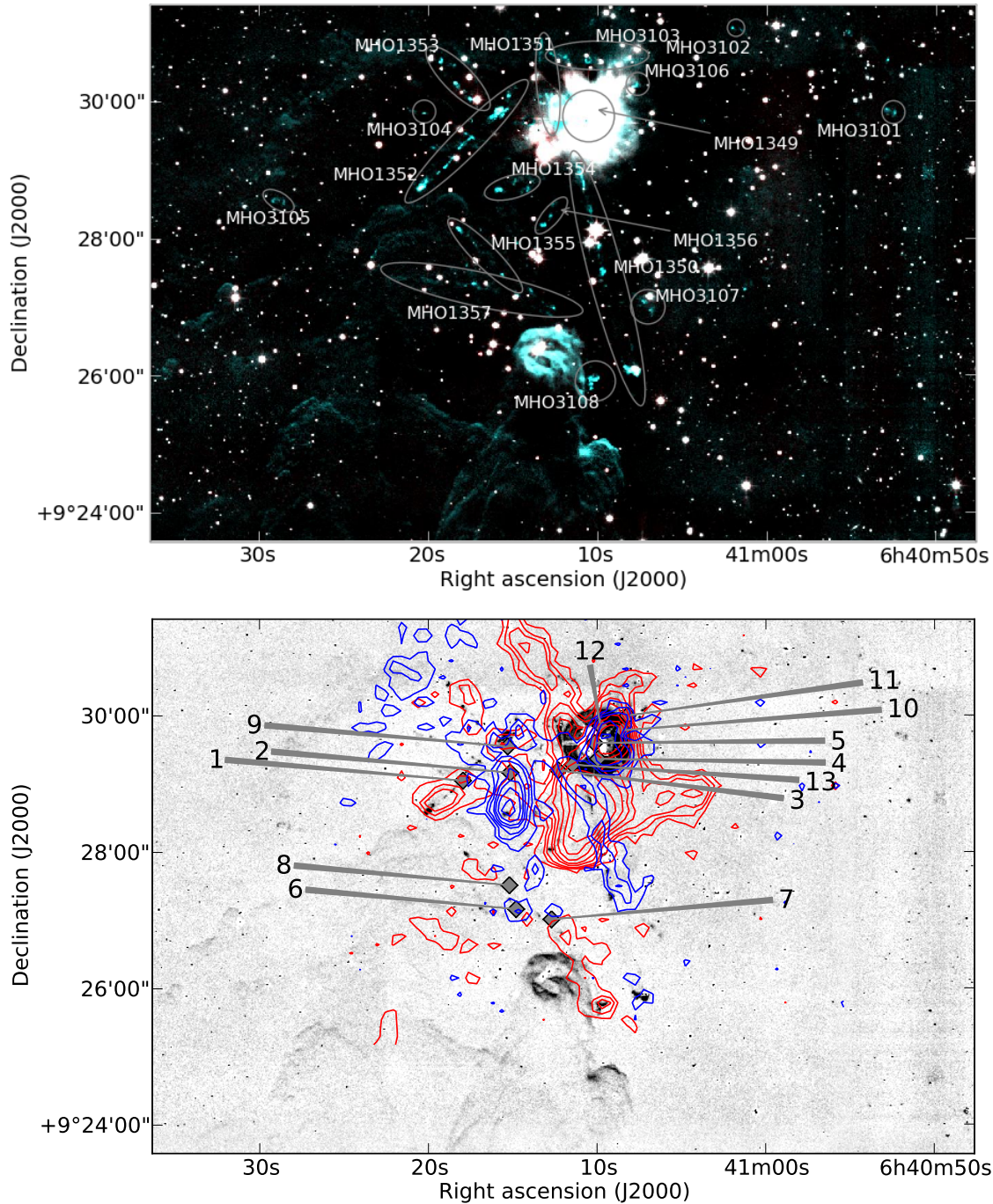


Figure 13. Top: H₂ colour composite image of NGC 2264 C, as Fig. 3. Bottom: Red and blue shifted CO emission contoured over the H₂ continuum-subtracted greyscale image. Contours are at 3.9, 6.5, 9.1, 14.3, 19.5, 27.3, 37.7, 48.1 K km s⁻¹. Red-shifted emission extends from 12.2 to 30.9 km s⁻¹, and the blue-shifted from -17.8 to 2.1 km s⁻¹. The saturated source seen in the H₂ emission is Allen’s source (Allen 1972). The sources identified by Peretto et al. (2006) are marked and labeled with the CMM number.

The jet, shows a curved chain of features, extends southwards from CMM3, and so we tentatively assign this as the driving source. The lobes can’t be traced directly back to the source due to the overlapping flows in the central regions.

CMM7, previously identified as prestellar, is at the base of a bipolar molecular outflow and associated bow shocks, MHO3108 and MHO1354. CMM7 is also associated with a *Spitzer* 24 μm identified protostar, 13822 (Sung et al. 2009). CMM6 is co-

incident with a chain of H₂ knots ending in a bow shock in MHO1355, associated with red-shifted emission. There is also a small extension of H₂ knots seen associated with blue-shifted emission on the other side of the source. If this jet extends any further, the emission is not distinguishable from the emission extending from the Cone Nebula. CMM8 is located between two small red- and blue-shifted emission regions which it may be driving, although there is also an H₂ emission knot perpendicular to the line

Source	H ₂		CO lobes		length (")	
	Red	Blue	Red	Blue	Red	Blue
CMM1	MHO1352		Y	Y	45	58
CMM2	MHO1304		?	Y		92
CMM3	MHO1356		Y	?	75	
CMM6	MHO1355		Y	Y	67	14
CMM7	MHO3108	MHO1354	Y	Y	90	100
CMM8	?	?	Y	Y	31	20
CMM9	MHO1353		Y	?	77	
CMM10/13288 ^a	MHO3106		Y	?		
CMM13	MHO1351	MHO1350	Y	Y	126	124
13350 ^a	MHO1303		Y	N	41	46
14314 ^a /14415 ^a	MHO1357		?	?		

^a Identification from Sung et al. (2009)

Table 4. Driving source identifications for NGC 2264 C flows.

of the outflow lobes, at a similar distance to the source. There is a *Spitzer*-identified protostar at this location, 14314. MHO1357 is spatially co-incident with the two Class I *Spitzer* identified sources, 14314 and 14415 (Sung et al. 2009) separated by just 11". The sources and outflows in this region are closely clustered, and driving jets and outflows in different directions. This small cluster of cores (CMM6, CMM7 and CMM8) is surrounded by compact H₂ emission, and it is difficult to definitively assign all of the emission to one source or another. The amount of H₂ emission and red- and blue-shifted CO emission does suggest that these cores are protostellar, rather than prestellar as previously catalogued.

CMM9 has been identified as prestellar by (Peretto et al. 2006), but we see evidence of a chain of H₂ knots, MHO1353, and weak red-shifted emission associated with this source, perpendicular to the blue-shifted outflow lobe from CMM1. Any blue-shifted emission that may be associated with this source is entangled with the blue outflow lobe from CMM1. There is a *Spitzer* 24 μ m identified protostar, 14214 (Sung et al. 2009) 11" from CMM9, which is spatially coincident with the terminal bow shock from the blue-shifted lobe of CMM1.

CMM10 is close to a *Spitzer* 24 μ m Class I source (13288 Sung et al. 2009), very close to IRS1, which is saturating the H₂ image. The *Spitzer* peak is spatially most closely aligned with the red outflow lobe, and is close, although not coincident with CMM10. There is also two compact H₂ knots, MHO1306, which align with this source and red-shifted emission. Therefore, we tentatively identify CMM10 as the driving source of this flow. Any blue-shifted emission is co-incident with the energetic flows at the centre of the cluster, and not easily distinguishable.

CMM13 has a spectacular bipolar jet and molecular outflow, and has a particularly clear jet and multiple bow-shocks, MHO3107, associated with the blue-shifted lobe. The red-shifted lobe is coincident with MHO1351.

The remaining CMM sources are all tightly clustered near Allen's Source, which drives an energetic bipolar flow, and is saturated in the H₂ emission, making it difficult to establish individual flows.

7.3 The protostellar content of NGC 2264 D

NGC 2264 D is less luminous than NGC 2264 C, forming several intermediate/high mass stars (Peretto et al. 2006) with core masses of 1.9–17.3 M_⊙, estimated from submillimetre observations. The submillimetre sources are less clustered than in NGC 2264 C, but

high resolution observations (Sung et al. 2009; Teixeira et al. 2006) show many of the submillimetre sources are co-incident with multiple tightly clustered protostars. Forbrich et al. (2010) detects PAH emission surrounding 3 embedded YSOs in NGC 2264 D, making them candidate massive YSOs. We investigate the protostellar status of these objects using our CO and H₂ data. All of the candidates, SSB 1070, SSB 11829 and SSB 12820 are associated with compact K-band continuum sources. SSB 11829 is co-incident with a ¹²CO bipolar molecular outflow, and MHO 1385, a bright knot and extended west-facing bow shock, indicating the source is protostellar. A second, SSB 10710, has a very faint H₂ emission knot to the west, although this is not a sufficiently significant detection to be identified as an MHO, and we do not detect any clear outflow signatures in ¹²CO that we can identify with this source.

Eleven prestellar and four protostellar cores have been identified by Peretto et al. (2006), and we have adopted their labelling scheme of, labelling the cores DMM1–DMM15. Fig. 14 shows the red- and blue shifted contours overlaid on the H₂ emission, as Fig. 6, with the DMM sources also labelled. Six of the prestellar cores are co-incident with *Spitzer* 24 μ m identified protostars (Sung et al. 2009), and two of these show clear outflow structure in CO emission, DMM2 and DMM13. Both of these are part of a ridge containing a previously identified protostellar source, DMM7. The final source in this ridge, DMM15 is also associated with a 24 μ m source, but only has weak evidence of outflow activity. The NGC 2264 D cluster is more tightly clustered than NGC 2264 C, and many of the DMM sources are co-located with multiple *Spitzer* identified protostars, making it difficult to isolate individual flows. Where this has been possible, we list in Table. 5 the CO outflows and MHOs we have been able to associate with a driving source, and the lengths of the flows, measured from either the H₂ emission, or from CO red- or blue-shifted emission. We describe the flows in more detail below.

The area surrounding MHO1385 contains two prestellar cores, DMM4 and DMM6, and 4 *Spitzer*-identified protostars (Sung et al. 2009), one of which is co-incident with an H₂ knot. MHO1385 is associated with mainly blue-shifted emission, with a more compact, slightly overlapping red-shifted CO flow to the west. Although there are multiple sources in this region, the bipolar flow is not obviously associated with any of the nearby sources or H₂ emission. Midway between DMM4 and DMM6 lies a candidate massive YSO, SSB 11829 (Smith et al. 2010), and it is this source that is spatially aligned with the molecular outflow and MHO 1385. 50" to the south-east of MHO1385 are two more H₂ objects, MHO1383 and MHO1384, two prestellar cores, DMM2 and DMM15, and 5 *Spitzer*-identified protostars, all within a radius of 30". There is red- and blue-shifted emission associated with this region, but it is not possible to disentangle individual flows at this resolution. DMM7 is located at the base of MHO1386, which is clearly associated with blue-shifted emission, although we can't isolate any red-shifted counterpart to this flow.

MHO1380 is coincident with a compact peak of red-shifted CO emission. MHO1381 is associated with weak blue-shifted emission, and could be a counterpart. There is no known source associated with this flow, nor with MHO1382, which ends in a bright, knotty arc of emission. The shape of the arc suggests it is driving towards the cluster, not away from it. MHO1382 is associated with an extended red-shifted flow, with no detectable driving source. MHO1391 contains multiple arcs and knots of H₂ emission, each of the H₂ clusters associated with a peak of red-shifted CO emission - four in total. At the southern end of MHO1391, there is a compact blue-shifted emission region that overlaps the penultimate

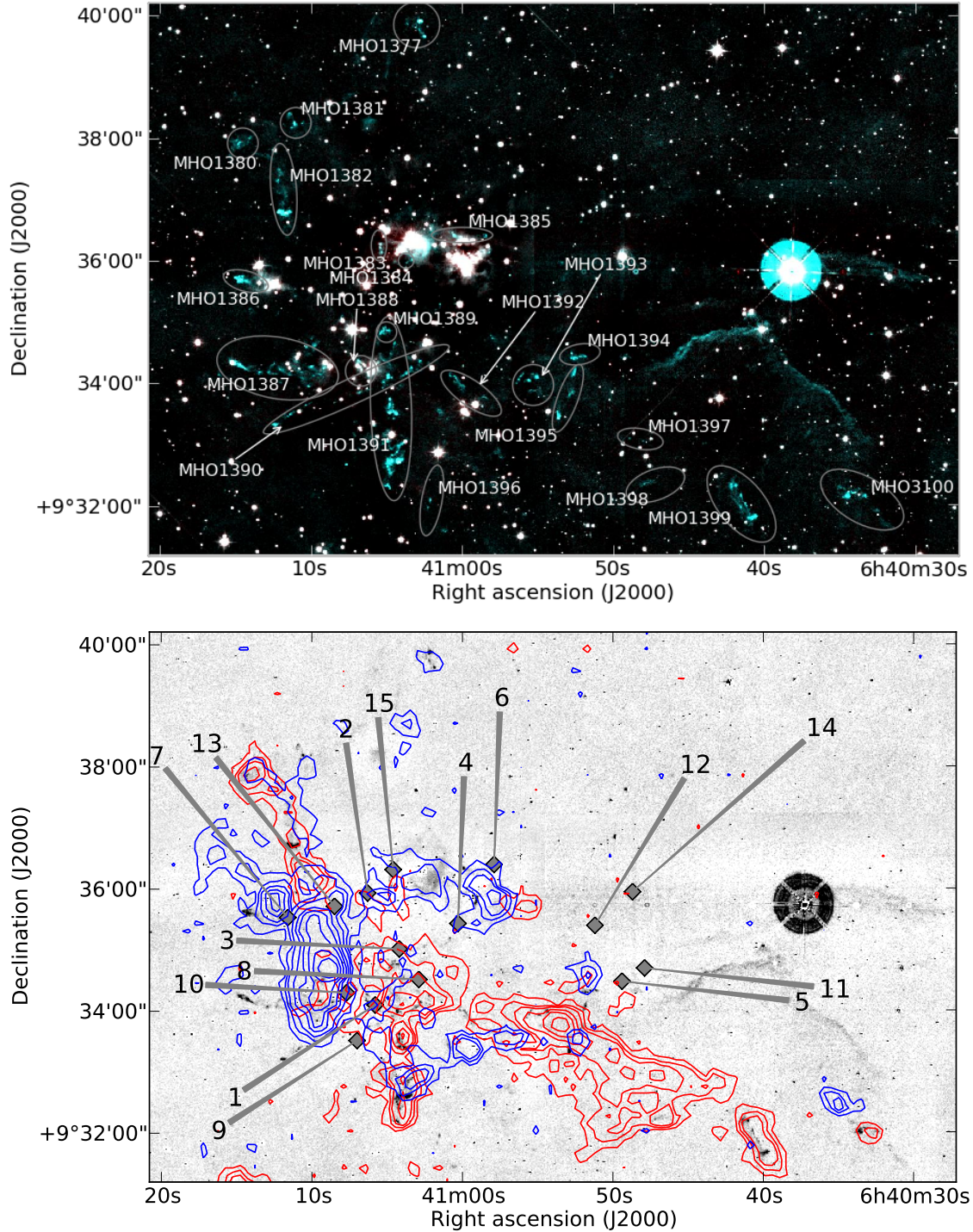


Figure 14. Top: H₂ colour composite of NGC 2264 D, as Fig. 3. Bottom: Red and blue shifted CO emission contoured over the H₂ continuum-subtracted greyscale image. Contours are at 3.9, 6.5, 9.1, 14.3, 19.5, 27.3, 37.7, 48.1 K km s⁻¹. Red-shifted emission extends from 11.1 to 25.5 km s⁻¹, and the blue-shifted from -18.5 to 1.0 km s⁻¹. The sources identified by Peretto et al. (2006) are marked and labeled with the DMM number.

red-shifted region. However, there is no source that is obviously driving these flows. There are no detected sources at the southern end of MHO1391, although there is a prestellar core, DMM8 to the north, and seven *Spitzer*-identified protostars to the north-east, near DMM1. DMM1, located within 8'' of 5 *Spitzer*-identified protostars, is also coincident with MHO1388.

MHO1392 is part of the dominant region of red-shifted emis-

sion that extends across ~8' to the south-west of NGC 2264 D. It is crossed by a double-peaked region of blue-shifted emission, although there is no nearby source detected that could be driving this flow. MHO1393, MHO1395 and MHO 1394 are also coincident with this long ridge of red-shifted emission, although the different alignments of the knots, jets and bow shocks associated with these MHOs indicate that they may be arising in smaller flows that we are

Source	H ₂		CO lobes		length (")	
	Red	Blue	Red	Blue	Red	Blue
DMM7		MHO1386	?	Y		45
-	MHO1380	MHO1381	Y	Y	42	17
-	MHO1382		Y		66	
-	MHO3100		Y	Y	35	52
12253 ^a		MHO1377	M	Y		19

^a Identification from Sung et al. (2009)

Table 5. Driving source identifications for NGC 2264 D flows.

not able to distinguish from the larger scale flow. Further along the large red-shifted flow, are several more MHOs, MHO1397, MHO 1398 and MHO1399, each of which are coincident with peaks in the red-shifted flow. At the south-west tail of the large red flow is a compact bipolar flow, that has MHO3100 associated with the red-shifted lobe. There is no detected driving source for this flow, but it does lie outside the SCUBA and *Spitzer* observed areas. To the north of NGC 2264 D, MHO1377 is coincident with a weak compact clump of blue-shifted emission, and a *Spitzer*-identified protostar, 12253 (Sung et al. 2009).